Temperature–field phase diagram of extreme magnetoresistance

Fazel Fallah Tafti[a], Quinn Gibson[a], Satya Kushwaha[a], Jason W. Krizan[a], Neel Haldolaarachchige[a], and Robert Joseph Cava[a,1]

[a]Department of Chemistry, Princeton University, Princeton, NJ 08544

Contributed by Robert Joseph Cava, May 9, 2016 (sent for review April 13, 2016; reviewed by A. D. Bianchi and Liang Fu)

The recent discovery of extreme magnetoresistance (XMR) in LaSb introduced lanthanum monopnictides as a new platform to study this effect in the absence of broken inversion symmetry or protected linear band crossing. In this work, we report XMR in LaBi. Through a comparative study of magnetotransport effects in LaBi and LaSb, we construct a temperature–field phase diagram with triangular shape that illustrates how a magnetic field tunes the electronic behavior in these materials. We show that the triangular phase diagram can be generalized to other topological semimetals with different crystal structures and different chemical compositions. By comparing our experimental results to band structure calculations, we suggest that XMR in LaBi and LaSb originates from a combination of compensated electron–hole pockets and a particular orbital texture on the electron pocket. Such orbital texture is likely to be a generic feature of various topological semimetals, giving rise to their small residual resistivity at zero field and subject to strong scattering induced by a magnetic field.

extreme magnetoresistance | topological semimetal | orbital texture

Materials with large magnetoresistance (MR) have applications in electronics as magnetic memories (1, 2), in spintronics as magnetic valves (3), and in industry as magnetic sensors or magnetic switches (4, 5). Recent reports of extreme magnetoresistance (XMR) in several nonmagnetic semimetals have attracted attention due to its distinction from giant and collosal MR in magnetic semiconductors (2, 6). XMR is observed in Dirac semimetals such as Na_3Bi or Cd_3As_2 (7, 8), Weyl semimetals such as NbP, NbAs, or TaAs (9–11), and layered semimetals such as WTe_2, $NbSb_2$, or $PtSn_4$ (12–16). The recent discovery of XMR in LaSb that does not belong to any of these categories shows that XMR is a ubiquitous phenomenon observed in seemingly unrelated materials (17). It also clearly underlines that the mechanism for XMR is not understood. The present article is a first attempt to unify the phenomenology of XMR in seemingly unrelated materials, to provide a common phase diagram for XMR, and to elucidate its underlying mechanism. We hope that this will enable theorists to develop a model capable of describing the underlying physics, once all of the salient experimental features are captured.

We report the discovery of XMR in LaBi with similar crystal structure and chemical composition to LaSb. Fig. 1 shows the simple rock salt structure of lanthanum monopnictides. Through a comparative study of longitudinal and transverse magnetotransport in LaSb and LaBi, we construct a characteristic triangular *T-H* phase diagram for XMR in lanthanum monopnictides. Our band structure calculations, quantum oscillations, and Hall Effect measurements suggest that XMR is rooted in a combination of compensated electron–hole pockets and a mixed orbital texture within the electron pockets. The orbital texture is a result of lanthanum *d* states crossing the pnictogen *p* states. Spin–orbit coupling then opens a small gap at the point of crossing to form the electron pocket with mixed *d*–*p* orbital texture. A recent theoretical work pointed to the topological nature of lanthanum monopnictides that results from this crossing (18). Here, we show that a similar orbital texture exists in other topological semimetals and so does the triangular *T-H* phase diagram. The finding of a universal phase diagram across materials with diverse structures and chemical compositions implies that XMR is a ubiquitous phenomenon and expected to be found in many more compounds.

Results

Temperature Dependence of Resistivity. Fig. 2 *A* and *B* shows the temperature dependence of resistivity in LaSb and LaBi. At $H = 9$ T (black curves), with decreasing temperature, resistivity decreases initially until a minimum at T_m, then increases until an inflection at T_i where it gradually saturates to a plateau. Fig. 2*B*, *Inset* shows that the resistivity upturn is absent at zero field. It is switched on with a small magnetic field $H_{\text{onset}} = 0.4 \pm 0.1$ T and becomes more prominent as the field increases, promising applications such as low-temperature magnetic switches and sensors.

Fig. 2*C* is a plot of $\partial\rho/\partial T$ versus T for LaBi that marks T_m as the temperature where $\partial\rho/\partial T$ changes sign and T_i as the temperature where $\partial\rho/\partial T$ shows a peak. With increasing field, T_m increases but T_i remains unchanged. Fig. 2*D* is an Arrhenius plot of $\log(\rho)$ versus T^{-1} for LaBi showing that, in the narrow region between T_m and T_i, resistivity fits to $\rho(T) \propto \exp(E_a/k_B T)$ where E_a is the activation energy and k_B is the Boltzmann constant. E_a is plotted as a function of field for LaSb and LaBi in Fig. 3 *C* and *D*. At first, such analysis may suggest a metal–insulator transition (MIT) at T_m, but, as we explain later, this is certainly not the case.

Significance

Extreme magnetoresistance (XMR) has been recently discovered in a number of seemingly unrelated materials with diverse crystalline and electronic structures. In this work, we use lanthanum monopnictides, LaBi and LaSb, as simple platforms to reveal a common triangular Temperature–field phase diagram for XMR. Further, we show that, in the electronic structure of both materials, lanthanum *d* orbitals mix with the pnictogen *p* orbitals. Remarkably, we find that both the triangular phase diagram and the orbital texture exist in all families of semimetals with XMR. These results show that XMR is a ubiquitous phenomenon with a universal phase diagram that goes beyond certain material specifications; it is not a rare commodity of topological materials or noncentrosymmetric structures.

Author contributions: F.F.T. and R.J.C. designed research; F.F.T., S.K., and N.H. performed research; F.F.T. contributed new reagents/analytic tools; F.F.T., Q.G., and J.W.K. analyzed data; and F.F.T., Q.G., and R.J.C. wrote the paper.

Reviewers: A.D.B., Université de Montréal; and L.F., Massachusetts Institute of Technology.

Conflict of interest statement: R.J.C. and A. D. Bianchi have appeared as coauthors in a different topic area in the previous publication by Fennell A, et al. (2014) Evidence for $SrHo_2O_4$ and $SrDy_2O_4$ as model J_1-J_2 zigzag chain materials. *Phys Rev B* 89(22):224511. In that collaboration, samples synthesized in R.J.C. laboratory by T. Klimczuk were sent directly to M. Kenzelman for experimental study. R.J.C., Bianchi, and Kenzelman work at separate institutions and R.J.C. and Bianchi did not have any contact during the course of that work.

[1]To whom correspondence should be addressed. Email: rcava@princeton.edu.

This article contains supporting information online at www.pnas.org/lookup/suppl/doi:10.1073/pnas.1607319113/-/DCSupplemental.

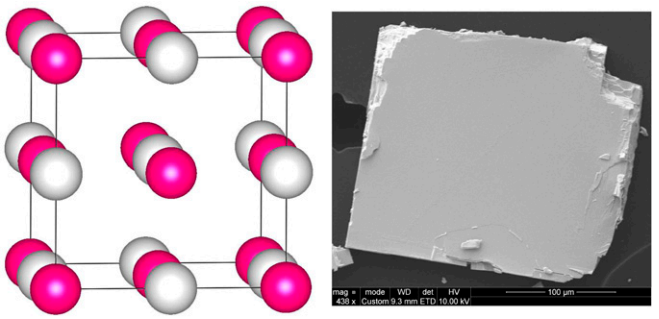

Fig. 1. (*Left*) NaCl-type crystal structure of LaSb/LaBi with space group $Fm\bar{3}m$. Gray spheres represent La, and pink spheres represent Sb/Bi. (*Right*) Scanning Electron Microscopy image of LaBi single crystal showing cubic symmetry and the cleaved [100] surface. X-ray refinements are presented in *Supporting Information*.

Phase Diagram. By plotting T_m and T_i as a function of magnetic field, we construct the temperature–field phase diagram of XMR in LaSb and LaBi (Fig. 3 *A* and *B*). In both systems, T_m increases with increasing field whereas T_i stays unchanged. The shaded triangle between T_m and T_i marks the region of MR where $\partial\rho/\partial T < 0$ (Fig. 2*C*, *Inset*). The silver area above the triangle ($T > T_m$) in Fig. 3 *A* and *B* is the region of metallic conduction where $\partial\rho/\partial T > 0$ with negligible MR which is quadratic in field. The gold area below the triangle ($T < T_i$) is the plateau region where $\partial\rho/\partial T \to 0$. Toward the end of the paper, we will show that the triangular phase diagram is universal to all semimetals with XMR (see Fig. 9).

Fig. 3 shows that LaSb and LaBi have comparable E_a but different T_m. If an MIT was responsible for the resistivity upturn, then the smaller T_m in LaBi should have translated to a smaller E_a. Additional evidence against an MIT comes from a comparison of the electronic specific heat in $H = 0$ and in an applied field of $H = 9$ T (Fig. S1). Recent work on another XMR material, WTe_2, has also ruled out field-induced MIT at T_m through a scaling analysis and the use of Kohler's rule (19, 20). In the absence of an MIT, the resistivity upturn at T_m must result from a strong field-induced scattering. We will elaborate on such scattering process after discussing the band structure of LaBi and LaSb.

Field Dependence of Resistivity and XMR. Fig. 4 *A* and *B* shows MR = $100 \times [R(H) - R(0)]/R(0)$, as a function of magnetic field from $H = 0$ T to 9 T at several temperatures. The black and the yellow curves at $T = 2$ K and 5 K superimpose because both curves are in the plateau region where MR reaches its extreme limit in excess of 10^5%. Comparing Fig. 4 *A* and *B* with the phase diagram Fig. 3 *A* and *B* shows that MR is small in the conventional metallic region at $T > T_m$, it starts to increase in the region of field-induced scattering at $T_i < T < T_m$, and it reaches the extreme limit in the plateau region at $T < T_i$. Ref. 17 shows that the magnitude of XMR is sensitive to the residual resistivity ratio (RRR), i.e., to the sample quality. We quote RRR values for the LaSb and the LaBi samples in Fig. 4 *A* and *B* to prevent the reader from taking away the wrong conclusion that the XMR in LaSb is smaller than in LaBi. Fig. 4*C* is a plot of MR as a function of RRR for several LaSb and LaBi specimens with different RRR values. MR in both materials follows the same quadratic dependence on RRR, showing a comparable XMR in both compounds given comparable sample quality. A similar quadratic dependence of XMR on RRR is reported in the flux-grown WTe_2 samples (13).

The ripples in the resistivity at higher fields in Fig. 4 *A* and *B* are Shubnikov–de Haas (SdH) oscillations. The purely oscillatory part of resistivity $\Delta\rho(H)$ is obtained by subtracting a smooth H^2 background from $\rho(H)$ in the range from $H = 6$–9 T. $\Delta\rho$ is periodic in H^{-1} as seen in Fig. 4*D*, *Inset*. Fast Fourier Transform (FFT) of these data gives a peak at $F_0 = 271 \pm 5$ T in Fig. 4*D* for LaBi. Similar analysis gives $F_0 = 212 \pm 5$ T for LaSb (17). The principal frequencies for LaSb and LaBi do not match the known frequencies of tin and indium, ruling out flux inclusion (21, 22).

Angle Dependence of XMR and SdH Oscillations. Fig. 5 *A* and *B* shows the angle dependence of XMR in LaSb and LaBi. The direction of magnetic field H and electrical current I with respect to [100] crystal plane is shown schematically. XMR is maximum when $H \perp I$ and minimum when $H \| I$. It remains positive at all angles. Fig. 5 *C* and *D* shows that the principal frequency in LaSb and LaBi has the following angle dependence:

$$F = \frac{F_0}{\cos\left(\theta - \frac{n\pi}{2}\right)} \qquad [1]$$

where n is an integer, θ is the angle, and F_0 is the principal frequency at $\theta = 0$. Such angle dependence describes either a strictly 2D Fermi surface such as TI surface modes (25–27) or a quasi-2D bulk state such as the prolate ellipsoidal geometry of the electron pocket in lanthanum monopnictides (Fig. 6 *C* and *D*). Fig. 5*C* shows perfect agreement between our data and prior studies of magnetic oscillations (gray symbols) (23, 24, 28, 29).

Band Structure and the Orbital Texture. Fig. 6 *A* and *B* shows the results of our band structure calculations on LaSb and LaBi with the WIEN2k code using the full relativistic treatment of spin–orbit coupling (30). In both systems, two hole bands at the Γ point and one electron band near the X point cross the Fermi level E_F. Fig. 6 *C* and *D* visualize the corresponding Fermi surfaces with the two

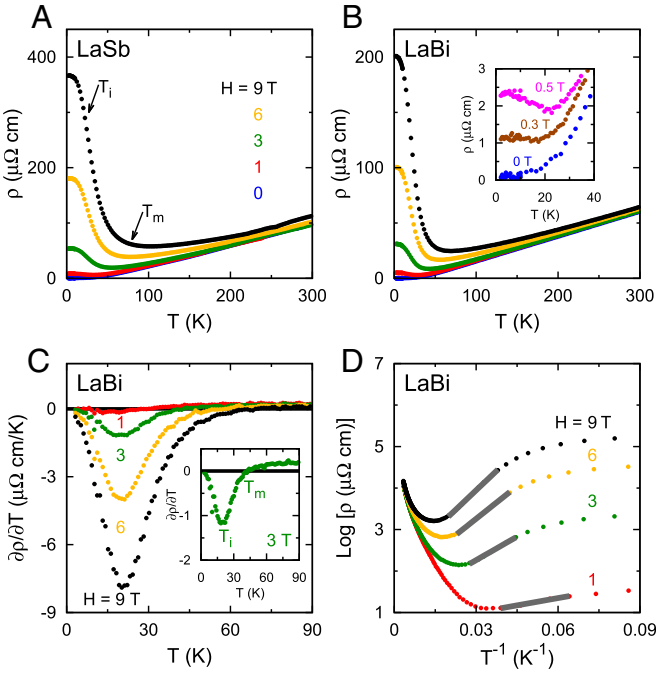

Fig. 2. (*A*) Resistivity as a function of temperature in LaSb at several magnetic fields as indicated on the figure. Temperature of resistivity minimum T_m and inflection T_i are marked on the black curve at $H = 9$ T. (*B*) The $\rho(T)$ in LaBi at the same fields as in LaSb. *Inset* shows $\rho(T)$ at low T and low H with the onset of resistivity upturn at $H_{onset} = 0.4 \pm 0.1$ T. (*C*) The $\partial\rho/\partial T$ as a function of temperature in several fields as indicated on the figure for LaBi. *Inset* shows the sign change temperature T_m and the peak temperature T_i for the green curve at $H = 3$ T. (*D*) Arrhenius plot of $\log(\rho)$ versus T^{-1} used to extract the activation energy E_a at several fields. The gray part of the traces indicates the temperature range used to extract the activation energy.

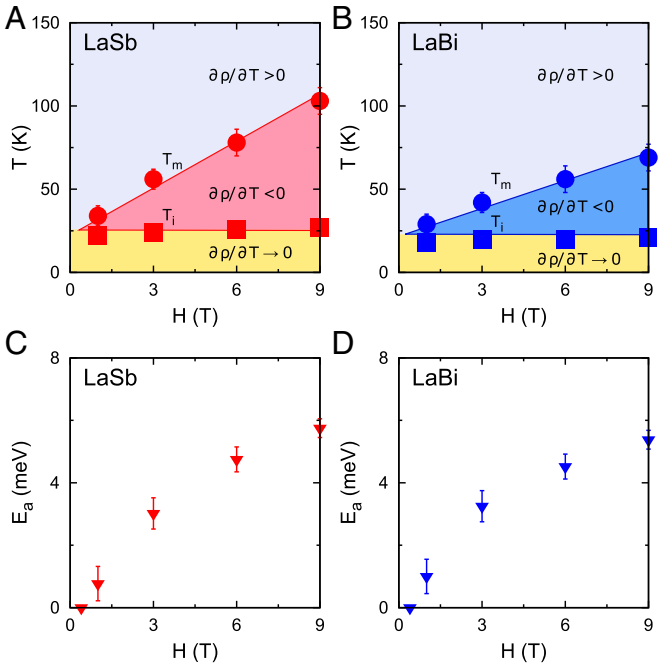

Fig. 3. (*A*) T_m (circles) and T_i (squares) plotted as a function of H in LaSb. For fields below $H_{onset} \simeq 0.4$ T, T_i and T_m are the same within our experimental precision, but they diverge for fields larger than H_{onset}. Although T_i is almost field-independent, T_m increases linearly over the measured field range. This gives rise to a triangular shape area in the *H-T* phase diagram where XMR occurs. The silver region above the circles is where $\rho(T)$ behaves like a conventional metal. The gold region below the squares is where $\rho(T)$ plateaus. (*B*) Similar triangular phase diagram for LaBi. (*C*) Activation energy E_a extracted from the Arrhenius analysis and plotted as a function of magnetic field for LaSb. Error bars represent maximum change of E_a by changing the fitting range. (*D*) E_a plotted as a function of field for LaBi.

hole surfaces at the center of the Brillouin zone and the ellipsoidal electron pockets crossing the faces. Prior studies of quantum oscillations in the magnetic and acoustic channels have mapped these hole and electron Fermi surfaces in both materials in detail (23, 24, 28, 29). The principal SdH frequencies that we observe in LaSb ($F_0 = 212$ T) and LaBi ($F_0 = 271$ T) match the cross-sectional area of the electron pocket at the X point.

We plot Antimony p states as thick bands and lanthanum d states as thin bands in Fig. 6 *A* and *B*. Notice the crossing between these bands near the X point. Spin–orbit coupling opens a small gap as shown in Fig. 6 *A* and *B*, *Insets* to form the electron pocket. The orbital character of momentum states changes from d to p as they wind around this electron pocket. Such winding of the orbital quantum number around the electron pocket could translate to a pseudospin that can interact with a magnetic field, giving rise to strong scattering and a large $\rho(H)$. Topological protection due to band inversion results in a remarkably small residual resistivity, as low as $\rho(0) = 30$ nΩ·cm, at $H = 0$. The result is a very large $\rho(H)/\rho(0)$ known as XMR. A similar mechanism seems to be responsible for XMR in graphene, where the pseudospin originates from the mixing between valley degrees of freedom instead of orbital degrees of freedom (31–33).

Effective Mass and Dingle Temperature. Using the Onsager relation, $F = (\phi_0/2\pi^2)A_{ext}$ and $A_{ext} = \pi k_F^2$, we extract the Fermi wave vector and the density of carriers on the ellipsoidal electron pocket from the frequency of SdH oscillations. Here, ϕ_0, A_{ext}, and k_F are the quantum of flux, the extremal orbit area, and the Fermi wave vector. SdH frequencies and the corresponding values of k_F and n_e are summarized in Table 1 for LaSb and LaBi. The amplitude of oscillations damps with increasing temperature and with decreasing magnetic field (Fig. 4*D*) according to

$$\Delta\rho = R_L R_D \sin\left(\frac{2\pi F}{H} + \phi\right). \quad [2]$$

R_L is the Lifshitz–Kosevich factor that captures damping with increasing temperature,

$$R_L = \frac{X}{\sinh(X)}, \quad X = \frac{\alpha T m^*}{H} \quad [3]$$

where $\alpha = 2\pi^2 k_B m_e/e\hbar$ is a constant containing Boltzmann factor k_B, bare electron mass m_e, electron charge e, and reduced Plank constant $\hbar$. Here, m^* is the effective electron mass in units of m_e. R_D is the Dingle factor that captures damping with decreasing field,

$$R_D = \exp(-X_D), \quad X_D = \frac{\alpha T_D m^*}{H} \quad [4]$$

where T_D is the Dingle temperature from which the relaxation rate τ, the mean free path ℓ, and the mobility μ of charge carriers can be determined using

$$k_B T_D = \frac{\hbar}{2\pi\tau}, \quad \ell = v_F\tau, \quad \mu = \frac{e\tau}{m^*} \quad [5]$$

with the Fermi velocity $v_F = \hbar k_F/m^*$.

Fig. 7 *A* and *B* shows the Lifshitz–Kosevich fit (Eq. **3**) to the temperature dependence of the oscillation amplitude. The resulting effective masses are $m^* = 0.22\ m_e$ for LaSb and $m^* = 0.35\ m_e$

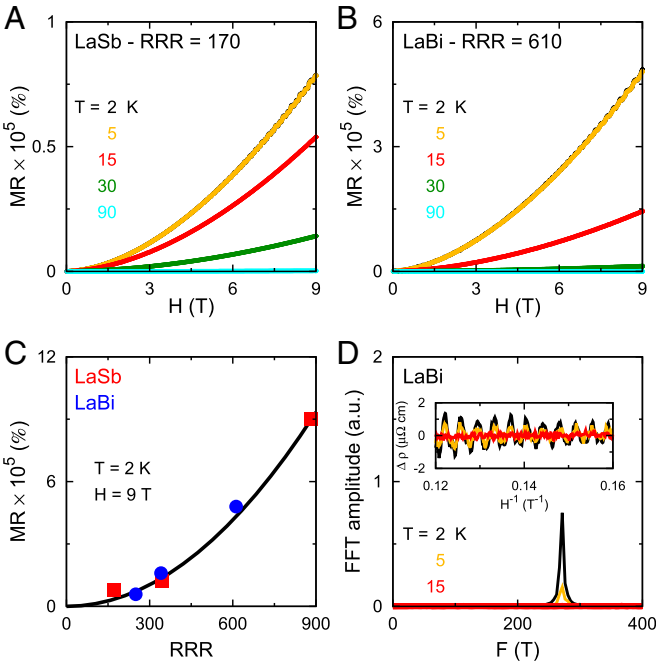

Fig. 4. (*A*) MR as a function of field in LaSb sample with RRR = 170 at several temperatures indicated on the figure. SdH oscillations appear at higher fields. (*B*) MR as a function of field for LaBi sample with RRR = 610. (*C*) MR at $T = 2$ K and $H = 9$ T plotted as a function of RRR for several LaSb (square) and LaBi (circle) samples. The solid black line is a quadratic fit that correlates RRR and XMR: Samples with larger RRR (smaller ρ_0) have larger XMR. (*D*) *Inset* shows the oscillatory part of resistivity, $\Delta\rho(H^{-1})$, at several temperatures for LaBi. FFT of these data are plotted as a function of frequency with a peak at $F_0 = 217$ T.

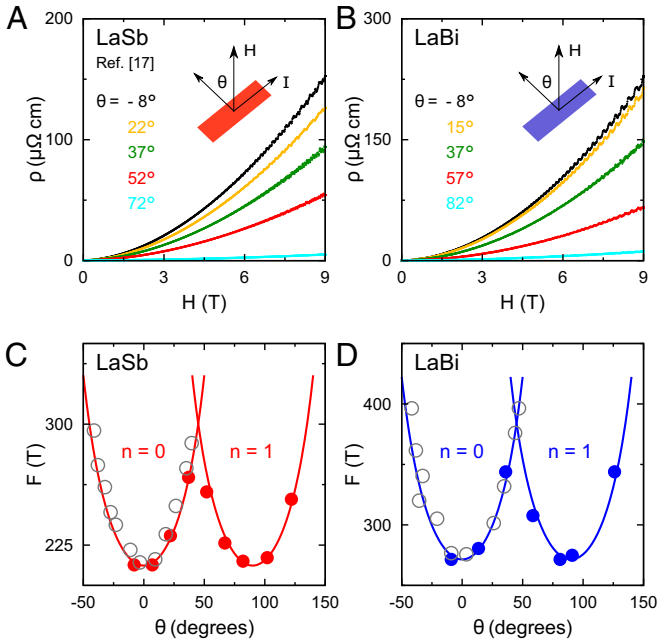

Fig. 5. (*A*) Resistivity as a function of magnetic field in LaSb at five representative angles as indicated. MR decreases with increasing θ. LaSb data are adapted from ref. 17. (*B*) The $\rho(H)$ in LaBi at five representative angles as indicated. MR stays positive at all angles in both systems. (*C*) SdH frequency as a function of angle in LaSb. Open gray circles are de Haas-van Alphen (dHvA) data from ref. 23. Solid lines are fits to Eq. **1** with $F_0 = 212$ T. (*D*) SdH oscillation frequency as a function of angle in LaBi. Solid lines are fits to Eq. **1** with $F_0 = 271$ T. Open gray symbols are dHvA data from ref. 24.

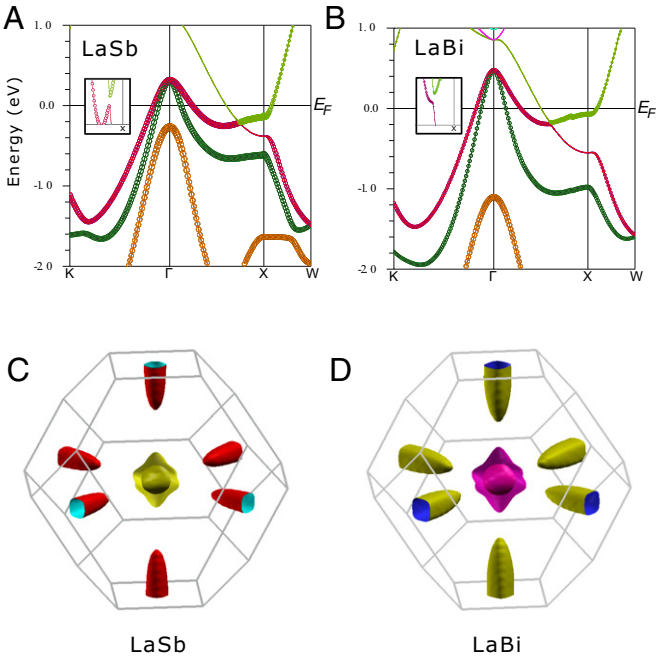

Fig. 6. (*A*) Band structure of LaSb with two hole pockets that cross E_F near Γ and one electron pocket that crosses E_F near *X*. The crossing between La *d* states (thin bands) and Sb *p* states (thick bands) near *X* gives a *d*–*p* texture to the electron pocket. *Inset* shows a small gap at this crossing due to spin–orbit coupling. (*B*) Band structure of LaBi with the same *d*–*p* crossing between La thin bands and Bi thick bands near *X*. *Inset* shows a small gap at this crossing due to spin-orbit coupling. (*C*) Fermi surfaces of LaSb in the first Brillouin zone with the central hole pockets and the peripheral electron pockets (prolate ellipsoids). SdH frequencies in Fig. 5 correspond to ellipsoidal electron pockets. (*D*) Similar Fermi surfaces of LaBi.

for LaBi, in agreement with calculations and previous works (23, 24, 28, 29). Fig. 7 *C* and *D* shows the Dingle fit (Eq. **4**) to the field dependence of the oscillation amplitude that determines τ, ℓ, and μ for the electron pockets in LaSb and LaBi. Table 1 summarizes all of the parameters from SdH oscillations.

Hall Effect and Electron–Hole Compensation. Fig. 8 shows the temperature dependence of Hall coefficient $R_H = \rho_{xy}/H$ at $H = 9$ T in LaSb (red) and LaBi (blue). Both materials show signatures of electron–hole compensation that results in a sign change in LaBi with positive R_H above $T \simeq 20$ K and negative R_H of comparable magnitude below $T \simeq 20$ K. LaSb shows a lesser degree of compensation, with a strong negative R_H signal below $T \simeq 40$ K and a weak positive signal above $T \simeq 40$ K that undergoes a second sign change at $T \simeq 170$ K. Although LaBi has better compensation, its XMR is typically smaller than LaSb, showing that the degree of compensation does not determine the magnitude of XMR. A key factor in determining the magnitude of XMR is the small residual resistivity that minimizes the denominator in the ratio $\rho(H)/\rho(0)$ (Fig. 4*C*).

Our hypothesis is that the orbital texture of electron Fermi surfaces results in the small $\rho(0)$ due to topological protection. It also results in the large $\rho(H)$ due to the interference of magnetic field with *d*–*p* mixing. Electron–hole compensation is certainly beneficial to XMR, but it only contributes to the large $\rho(H)$, not to the small $\rho(0)$. A small $\rho(0)$ is observed in all XMR materials such as WTe_2 or Cd_3As_2. These metals are typically prone to disorder due to their large and complex unit cells, yet they have some of the smallest residual resistivity known to metals. The source of such small ρ_0 (high mobility) is not clear, and it is perhaps the key to understanding the origin of XMR.

Fig. 8, *Inset* shows power law fits of the form $\rho = \rho_0 + AT^4$ to the resistivity data at low temperatures from which we extract residual resistivity $\rho_0 = 0.1$ μΩ·cm in LaBi and $\rho_0 = 0.6$ μΩ·cm in LaSb. Using the $T = 0$ limits of R_H and ρ_0 from Fig. 8, we estimate the Hall mobility from the single-band expression $\mu_{\text{Hall}} = R_H/\rho_0 = 3.2 \times 10^4$ $\text{cm}^2 \cdot \text{V}^{-1} \cdot \text{s}^{-1}$ in LaSb and $\mu_{\text{Hall}} = 2.5 \times 10^4$ $\text{cm}^2 \cdot \text{V}^{-1} \cdot \text{s}^{-1}$ in LaBi. Single-band estimates need to be taken with caution due to the multiband nature of these materials, but, qualitatively, they show extremely high mobility in all XMR materials. In *Supporting Information*, we show two-band model fits to the field dependence of R_H in both materials, from which the mobility and concentration of holes and electrons are extracted (Fig. S2 and Table S1).

Discussion

Our results in LaSb and LaBi can be summarized as follows: (*i*) The $\rho(T)$ at zero field shows a nearly perfect metal with very small ρ_0 (Fig. 2). (*ii*) The $\rho(T)$ in field shows strong field-induced

Table 1. Parameters from quantum oscillations

Material	F, T	m^*/m_e	T_D, K	k_F, cm^{-1}	n_e, cm^{-3}	v_F, $\text{cm} \cdot \text{s}^{-1}$	τ, s	ℓ, nm	μ_e, $\text{cm}^2 \cdot \text{V}^{-1} \cdot \text{s}^{-1}$
LaSb	212	0.22	7.8	8.0×10^6	1.6×10^{20}	4.2×10^7	1.6×10^{-13}	66	1,250
LaBi	271	0.35	3.7	9.1×10^6	2.0×10^{20}	3.0×10^7	3.3×10^{-13}	98	1,650

Electron Fermi surface parameters are tabulated for LaSb and LaBi from quantum oscillations.

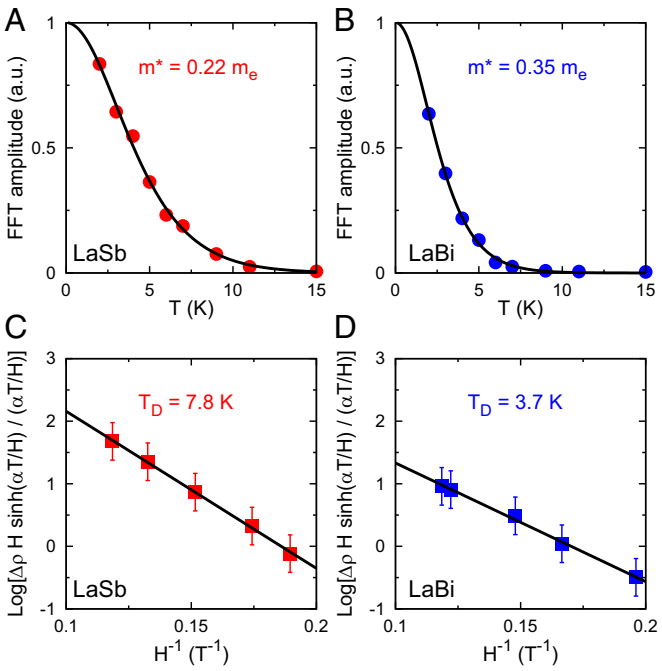

Fig. 7. (*A*) Amplitude of the FFT of SdH oscillations with $F_0 = 212$ T plotted as a function of temperature for LaSb. Solid line is a fit to the Lifshitz–Kosevich formula (Eq. **3**). The effective mass of carriers is extracted from the fit and reported on the figure. (*B*) Lifshitz–Kosevich analysis for LaBi. Effective mass in LaBi is slightly larger than LaSb. (*C*) FFT amplitudes modulated by the Lifshitz–Kosevich factor plotted as a function of H^{-1} for LaSb. Solid line is a fit to the Dingle formula (Eq. **4**). Dingle temperature T_D is reported on the figure. (*D*) Dingle analysis for LaBi.

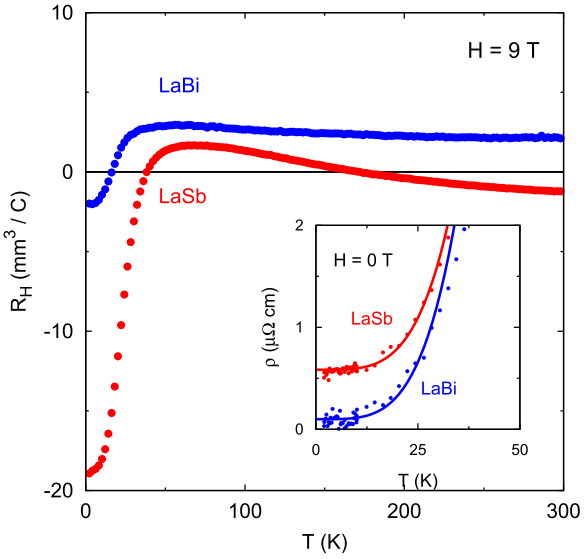

Fig. 8. R_H at $H = 9$ T plotted as a function of temperature from $T = 2$ to 300 K in LaSb (red) and LaBi (blue). There is one sign change in LaBi at $T \simeq 20$ K and two sign changes in LaSb at $T \simeq 40$ K and 170 K. *Inset* shows $\rho(T)$ at $H = 0$ T and $T < 40$ K in LaSb and LaBi. Solid lines are fits of the form $\rho = \rho_0 + AT^4$ to determine $\rho_0 = 0.6$ μΩ·cm in LaSb and 0.1 μΩ cm in LaBi.

scattering below T_m and a plateau below T_i (Fig. 2). (*iii*) The field dependence of T_m and T_i constructs a triangular phase diagram (Fig. 3). (*iv*) The strong field-induced scattering results in XMR that correlates with RRR (Fig. 4). (*v*) Angle dependence of SdH oscillations fits the ellipsoidal geometry of the electron Fermi surfaces (Fig. 5). (*vi*) From the band structure, these electron surfaces have a mixed d–p orbital texture (Fig. 6). XMR is possibly the consequence of disturbing such orbital texture with a magnetic field. (*vii*) The temperature and the field dependence of the Hall Effect fit to a two-band model with near compensation, but the degree of compensation does not justify the magnitude of XMR.

These results suggest that XMR in LaSb and LaBi originates from a combination of compensated band structure and a mixed orbital texture on electron pockets. The $\rho(T)$ and $\rho(H)$ profiles of XMR in seemingly different topological semimetals show similar features, with a resistivity minimum at T_m and inflection at T_i. From the existing transport data in $NbSb_2$ (15), $PtSn_4$ (16), and WTe_2 (12), we extract T_m and T_i, construct their T-H phase diagrams, and compare with the triangular phase diagram of LaBi in Fig. 9. Remarkably, the triangular phase diagram is universal to all materials with XMR, despite their chemical and structural differences. Identifying the fundamental energy scales related to T_m and T_i in the universal phase diagram of XMR remains an interesting open question.

Fig. 10 shows another universal feature: The same d–p orbital texture exists in the Fermiology of other semimetals with XMR including $NbSb_2$, $PtSn_4$, and WTe_2. Recent observations of circular dichroism by ARPES confirm such orbital mixing in WTe_2 (34). Fig. 9 unifies the phenomenology of XMR in various semimetals, and Fig. 10 links XMR to a combination of electron–hole compensation and mixed orbital texture. To emphasize the role of orbital texture, we highlight observations of XMR in single-band semimetals such as Cd_3As_2 and $Pb_{1-x}Sn_xSe$ that, by definition, cannot be compensated (8, 35). However, both systems show large degrees of orbital mixing in their electron

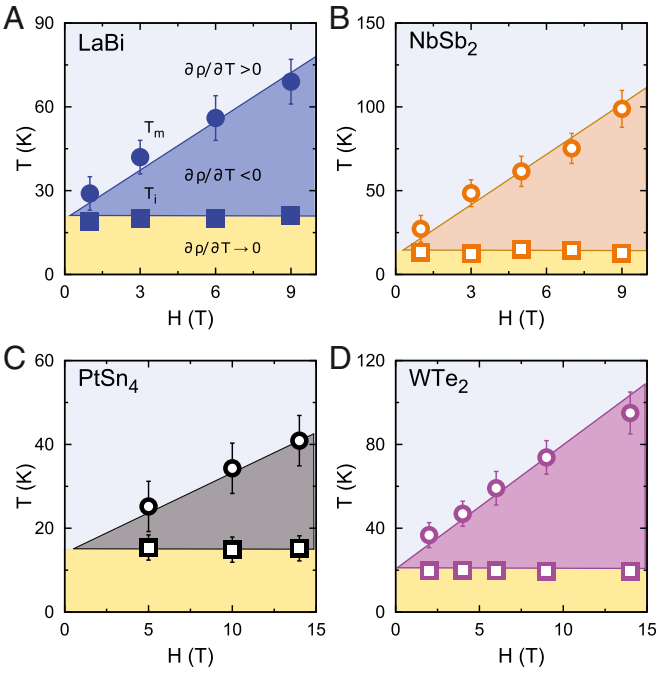

Fig. 9. (*A*) Triangular T-H phase diagram of LaBi, same as in Fig. 3*A*, compared with three different topological semimetals in the subsequent panels. (*B*) Triangular T-H phase diagram in $NbSb_2$ constructed with the data from ref. 15. T_m (circles) and T_i (squares) are the temperatures of resistivity minimum and inflection. Open symbols are used for all of the adapted data. (*C*) Triangular T-H phase diagram in $PtSn_4$ constructed with the data from ref. 16. (*D*) Triangular T-H phase diagram in WTe_2 constructed with the data from ref. 12. Aside from variations in the absolute values of T_m and T_i that depend on sample purity and XMR magnitude, these different topological semimetals share the same phase diagram.

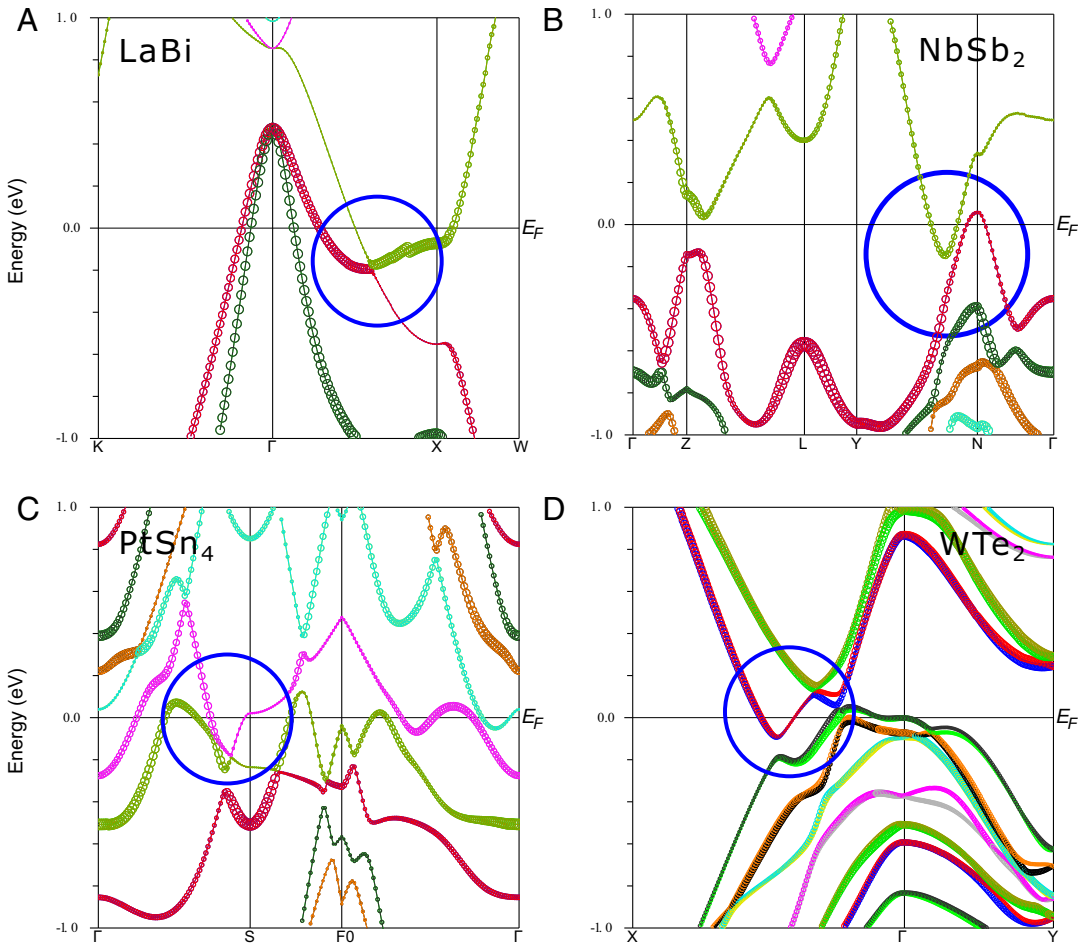

Fig. 10. (*A*) Band structure of LaBi, same as in Fig. 6*B*. The blue circle marks the region of *d*–*p* orbital mixing. (*B*) Band structure of $NbSb_2$ with a similar *d*–*p* mixing inside the blue circle. (*C*) Band structure of $PtSn_4$ with similar *d*–*p* mixing. (*D*) Band structure of WTe_2 with similar *d*–*p* mixing.

pockets that can interact with a magnetic field and result in the XMR. The extremely small residual resistivity of these systems ($\rho_0 = 1$ nΩ·cm in Cd_3As_2) despite their intrinsically disordered lattices is consistent with the topological protection proposed here.

Note that two recent works have reported XMR in LaBi (36, 37). Their data are in agreement with ours.

Materials and Methods

Single crystals of LaBi were grown using Indium flux. The starting elements La:Bi:In = 1:1:20 with purity 99.999% were placed in an alumina crucible inside an evacuated quartz tube. The mixture was heated to 1,000 °C, slowly cooled to 700 °C, and finally decanted in a centrifuge. A similar procedure was used to grow single crystals of LaSb from tin flux. Energy-dispersive X-ray spectroscopy on each sample confirmed a 1:1 ratio of lanthanum to pnictogen with ±1% error. Powder X-ray diffraction for both systems are presented in *Supporting Information* and Fig. S3. Resistivity measurements were performed in a Quantum Design Physical Property Measurement System using a standard four-probe method. Hall voltages were measured with transverse contacts in negative and positive fields, with the data antisymmetrized to calculate the transverse resistivity ρ_{xy} and the Hall coefficient $R_H = \rho_{xy}/H$. The LaSb single crystal had residual resistivity $\rho_0 = 0.6$ μΩ·cm and RRR $= \rho(300\text{ K})/\rho_0 = 170$. The LaBi crystal had $\rho_0 = 0.1$ μΩ·cm and RRR = 610.

ACKNOWLEDGMENTS. We thank G. Grissonanche, S. R. Julian, and L. Muechler for helpful discussions. This research was supported by the Gordon and Betty Moore Foundation under the EPiQS program, Grant GBMF 4412. S.K. is supported by the ARO MURI on topological insulators, Grant W911NF-12-1-0461.

1. Daughton JM (1999) GMR applications. *J Magn Magn Mater* 192(2):334–342.
2. Rao CNR, Cheetham AK (1996) Giant magnetoresistance in transition metal oxides. *Science* 272(5260):369–370.
3. Wolf SA, et al. (2001) Spintronics: A spin-based electronics vision for the future. *Science* 294(5546):1488–1495.
4. Lenz J (1990) A review of magnetic sensors. *Proc IEEE* 78(6):973–989.
5. Jankowski J, El-Ahmar S, Oszwaldowski M (2011) Hall sensors for extreme temperatures. *Sensors (Basel)* 11(1):876–885.
6. Ramirez AP (1997) Colossal magnetoresistance. *J Phys Condens Matter* 9(39): 8171–8199.
7. Xiong J, et al. (2015) Evidence for the chiral anomaly in the Dirac semimetal Na_3Bi. *Science* 350(6259):413–416.
8. Liang T, et al. (2015) Ultrahigh mobility and giant magnetoresistance in the Dirac semimetal Cd_3As_2. *Nat Mater* 14(3):280–284.
9. Shekhar C, et al. (2015) Extremely large magnetoresistance and ultrahigh mobility in the topological Weyl semimetal candidate NbP. *Nat Phys* 11(8):645–649.
10. Ghimire NJ, et al. (2015) Magnetotransport of single crystalline NbAs. *J Phys Condens Matter* 27(15):152201.
11. Huang X, et al. (2015) Observation of the chiral-anomaly-induced negative magnetoresistance in 3d Weyl semimetal TaAs. *Phys Rev X* 5(3):031023.
12. Ali MN, et al. (2014) Large, non-saturating magnetoresistance in WTe_2. *Nature* 514(7521):205–208.
13. Ali MN, et al. (2015) Correlation of crystal quality and extreme magnetoresistance of WTe_2. *Europhys Lett* 110(6):67002.
14. Zhu Z, et al. (2015) Quantum oscillations, thermoelectric coefficients, and the fermi surface of semimetallic WTe_2. *Phys Rev Lett* 114(17):176601.
15. Wang K, Graf D, Li L, Wang L, Petrovic C (2014) Anisotropic giant magnetoresistance in $NbSb_2$. *Sci Rep* 4:7328.
16. Mun E, et al. (2012) Magnetic field effects on transport properties of $PtSn_4$. *Phys Rev B* 85(3):035135.
17. Tafti FF, Gibson QD, Kushwaha SK, Haldolaarachchige N, Cava RJ (2016) Resistivity plateau and extreme magnetoresistance in LaSb. *Nat Phys* 12(3):272–277.

18. Zeng M, et al. (2015) Topological semimetals and topological insulators in rare earth monopnictides. arXiv:1504.03492.
19. Thoutam L, et al. (2015) Temperature-Dependent three-dimensional anisotropy of the magnetoresistance in WTe_2. *Phys Rev Lett* 115(4):046602.
20. Wang YL, et al. (2015) Origin of the turn-on temperature behavior in WTe_2. *Phys Rev B* 92(18):180402.
21. Deacon JM, Mackinnon L (1973) Ultrasonic quantum oscillations in white tin. *J Phys F Met Phys* 3(12):2082–2091.
22. Cowey JE, Gerber R, Mackinnon L (1974) Quantum oscillations in ultrasonic absorption and the Fermi surface of indium. *J Phys F Met Phys* 4(1):39.
23. Kitazawa H, et al. (1983) DE Haas-van Alphen effects on La(Sb, Bi) and Ce(Sb, Bi). *J Magn Magn Mater* 31-34(Part 1):421–422.
24. Hasegawa A (1985) Fermi Surface of LaSb and LaBi. *J Phys Soc Jpn* 54(2): 677–684.
25. Ren Z, Taskin AA, Sasaki S, Segawa K, Ando Y (2010) Large bulk resistivity and surface quantum oscillations in the topological insulator Bi_2Te_2Se. *Phys Rev B* 82(24):241306.
26. Li G, et al. (2014) Two-dimensional Fermi surfaces in Kondo insulator SmB_6. *Science* 346(6214):1208–1212.
27. Tan BS, et al. (2015) Unconventional Fermi surface in an insulating state. *Science* 349(6245):287–290.
28. Settai R, et al. (1993) Acoustic de Haas-Van Alphen effect in LaSb and CeSb. *Physica B* 186:176–178.
29. Yoshida M, et al. (2001) Cyclotron resonance of LaBi. *J Phys Soc Jpn* 70(7): 2078–2081.
30. Blaha P, Schwarz K, Madsen G, Kvasnicka D, Luitz J (2001) WIEN2K, An Augmented Plane Wave + Local Orbitals Program for Calculating Crystal Properties, ed Schwarz K (Tech Univ Wien, Vienna).
31. McCann E, et al. (2006) Weak-localization magnetoresistance and valley symmetry in graphene. *Phys Rev Lett* 97(14):146805.
32. Bai J, et al. (2010) Very large magnetoresistance in graphene nanoribbons. *Nat Nanotechnol* 5(9):655–659.
33. Xu X, Yao W, Xiao D, Heinz TF (2014) Spin and pseudospins in layered transition metal dichalcogenides. *Nat Phys* 10(5):343–350.
34. Jiang J, et al. (2015) Signature of strong spin-orbital coupling in the large non-saturating magnetoresistance material WTe_2. *Phys Rev Lett* 115(16):166601.
35. Liang T, et al. (2013) Evidence for massive bulk Dirac fermions in $Pb_{1-x}Sn_xSe$ from Nernst and thermopower experiments. *Nat Commun* 4(4):2696.
36. Sun S, Wang Q, Guo PJ, Liu K, Lei H (2016) Large magnetoresistance in LaBi: Origin of field-induced resistivity upturn and plateau in compensated semimetals. arXiv:1601.04618.
37. Kumar N, et al. (2016) Observation of quasi-two-dimensional electron transport in the topological semimetal LaBi. arXiv:1601.07494.